

Toward a unified theory for the Hadley cell descending and ascending edges

SPENCER A. HILL*

Program in Atmospheric and Oceanic Sciences, Princeton University, Princeton, New Jersey, and Lamont-Doherty Earth Observatory, Columbia University, Palisades, New York

SIMONA BORDONI

Department of Civil, Environmental and Mechanical Engineering (DICAM), University of Trento, Trento, Italy, and Division of Geological and Planetary Sciences, California Institute of Technology, Pasadena, California

JONATHAN L. MITCHELL

Department of Atmospheric and Oceanic Sciences, and Department of Earth, Planetary, and Space Sciences, University of California, Los Angeles

ABSTRACT

We present theories for the latitudinal extents of both Hadley cells throughout the annual cycle by combining our recent scaling for the ascending edge latitude (Hill et al. 2021) with the uniform Rossby number (Ro), baroclinic instability-based theory for the poleward, descending edge latitudes of Kang and Lu (2012). The resulting analytic expressions for all three Hadley cell edges are predictive except for diagnosed values of Ro and two proportionality constants. The theory captures the climatological annual cycle of the ascending and descending edges in an Earth-like simulation in an idealized aquaplanet general circulation model (GCM), provided the descending edge prediction is lagged by one month. In simulations in this and two other idealized GCMs with varied planetary rotation rate (Ω), the winter, descending edge of the solstitial, cross-equatorial Hadley cell scales approximately as $\Omega^{-1/2}$ and the summer, ascending edge as $\Omega^{-2/3}$, both in accordance with our theory.

1. Introduction

Climatologically over the annual cycle, the poleward, descending edges of the monthly Hadley cells vary meridionally by $\lesssim 5^\circ$ latitude about their annual mean positions, considerably less than the $\sim 15^\circ\text{S}$ – 15°N range of the shared, ascending edge Adam et al. (c.f. Fig. 4 of 2016)). Zonally averaged, this results in an intense seasonal cycle of rainfall in the deep tropics versus more consistently dry conditions in the subtropics. Regional deviations from the zonal average are pronounced—with for example intense Indian summer monsoon rainfall spanning roughly the same latitudes as the Sahara and Arabian deserts (Rodwell and Hoskins 1996)—nevertheless we focus on the zonal-mean problem, seeking a minimal explanation for these differing annual cycles of the descending and ascending edges (henceforth φ_d and φ_a respectively).

Our starting point for φ_d is the analytical model of Kang and Lu (2012, henceforth K12), whose own starting point is that of Held (2000, henceforth H00) for the annual-

mean φ_d that assumes the Hadley cells terminate where their zonal wind profiles become baroclinically unstable. KL12 extend the H00 model in two key ways. First, they generalize from the annual mean to the annual cycle by accounting, albeit diagnostically, for off-equatorial φ_a . For angular-momentum-conserving (AMC) zonal winds as assumed by H00, ascent off the equator results in weaker meridional shears (Lindzen and Hou 1988) and thus to baroclinic instability onset occurring farther poleward than for equatorial ascent. All else equal, this would cause φ_d to be farther poleward in solstitial seasons when φ_a is farthest from the equator compared to equinoctial seasons. Hilgenbrink and Hartmann (2018) utilize this conceptual framework to understand the response of the Hadley circulation annual cycle to perturbations in ocean heat transports.

Second, KL12 relax the H00 assumption of strictly AMC winds by assuming that the Rossby number (Ro) is uniform throughout each Hadley cell but not necessarily unity. Its formal definition follows below, but for now Ro is exactly unity for AMC winds and vanishes for vanishing zonal winds, and KL12 derive an analytical expression for the meridional profile of zonal wind under uniform

*Corresponding author address: Spencer Hill, 207B Oceanography, Lamont-Doherty Earth Observatory, 61 Route 9W, Palisades, NY 10964
E-mail: spencerh@princeton.edu

$0 < \text{Ro} \leq 1$. In simulations (Walker and Schneider 2006) and reanalysis data (Schneider 2006), Ro is regularly below unity and typically smaller in the equinoctial and summer cells than in the cross-equatorial winter cell (Bordoni and Schneider 2008; Schneider and Bordoni 2008). By diagnosing a bulk value of Ro for each cell and meteorological season in addition to φ_a , KL12 provide closed expressions for the northern and southern hemisphere descending edge latitudes in all four seasons.¹

To advance from diagnosing φ_a toward a closed theory, we recently presented a simple analytical scaling (Hill et al. 2021) in terms of the thermal Rossby number, which assumes that φ_a is determined by the meridional extent of supercritical radiative forcing into the summer hemisphere. In essence, in the present study we simply combine that scaling for φ_a with the KL12 model for φ_d (with slightly different assumptions about Ro compared to KL12 as detailed below). The result is a unified theory for φ_a and both hemispheres' φ_d with only two proportionality constants as well as Ro diagnosed (with a single Ro value for each cell and season).

Separately, in general circulation model (GCM) simulations with differing planetary rotation rates (Ω) the solstitial, cross-equatorial Hadley cell expands into both the summer and winter hemispheres as Ω decreases. In edying atmospheres φ_a is farther poleward than the winter φ_d for slowly rotating cases (e.g. Fig. 6 of Guendelman and Kaspi (2018)), whereas in Earth-like cases φ_a and the winter φ_d are nearly the same.² We will use our combined theory for φ_a and φ_d along with idealized GCM simulations to help explain this behavior.

In the following sections we:

- derive and describe fixed- Ro zonal wind, angular momentum, and depth-averaged potential temperature fields (Section 2);
- derive and describe our extension of the KL12 model for φ_d assuming fixed Ro and our theory for φ_a (Section 3);
- and test our theory over the annual cycle in a seasonally forced simulation in one idealized GCM and for the solstitial Hadley circulation in simulations at various rotation rates in three idealized GCMs (Section 4).

We then conclude with summary and discussion (Section 5).

2. Uniform- Ro fields

In general, absolute angular momentum is

$$M = a \cos \varphi (\Omega a \cos \varphi + u), \quad (1)$$

where a is planetary radius, φ is latitude, Ω is planetary rotation rate, and u is zonal velocity. This can be considered the sum of planetary angular momentum, $M_p(\varphi) \equiv \Omega a^2 \cos^2 \varphi$, and relative angular momentum $u a \cos \varphi$. If angular momentum is meridionally uniform and equal to the planetary angular momentum value at the latitude φ_a , $M_p(\varphi_a)$, the corresponding AMC zonal wind field is

$$u_{\text{amc}}(\varphi) = \Omega a \cos \varphi \left(\frac{\cos^2 \varphi_a}{\cos^2 \varphi} - 1 \right). \quad (2)$$

In the context of the Hadley cells, we equate φ_a in (2) with the cells' ascending edge on the grounds that ascent out of the viscous boundary layer there transmits the local planetary angular momentum, $M_p(\varphi_a)$, to the comparatively inviscid free troposphere (Held and Hou 1980; Lindzen and Hou 1988). This neglects the finite width of the ascent branch (Watt-Meyer and Frierson 2019; Byrne and Thomas 2019), but in principle one could compute an effective ascent latitude by averaging the planetary angular momentum over the full extent of the ascending branch, perhaps weighting by the vertical velocity out of the boundary layer at each latitude.

The Rossby number is defined as

$$\text{Ro} \equiv -\frac{\zeta}{f}, \quad (3)$$

where $\zeta \equiv -(\cos \varphi)^{-1} \partial_\varphi (u \cos \varphi)$ is relative vorticity and $f \equiv 2\Omega \sin \varphi$ is the planetary vorticity (i.e. the Coriolis parameter). Absolute vorticity is given by $\eta = f + \zeta = f(1 - \text{Ro})$. Absolute vorticity is proportional to the meridional gradient of angular momentum, and as such in an AMC state necessarily $\eta = 0$ and $\text{Ro} = 1$. In discussing the GCM simulations below, we will make use of a generalized version of Ro (Singh 2019), but (3) is the quantity used in the fixed- Ro fields we now define.

From (3), $\zeta = -\text{Ro} f$. If $\text{Ro} < 1$ but horizontally uniform, integrating meridionally yields the fixed- Ro zonal wind field,

$$u_{\text{Ro}}(\varphi) = \text{Ro} u_{\text{amc}}(\varphi), \quad (4)$$

which is simply the AMC zonal wind field scaled by Ro . The corresponding angular momentum field is

$$M_{\text{Ro}}(\varphi) = \Omega a^2 [(1 - \text{Ro}) \cos^2 \varphi + \text{Ro} \cos^2 \varphi_a], \quad (5)$$

which is a Ro -weighted average of the planetary angular momentum at the ascent latitude, $M_p(\varphi_a)$, and the full meridional distribution of the planetary angular momentum, $M_p(\varphi)$.

¹In addition to KL12, other authors have considered a uniform Ro in the tropical upper troposphere. Becker et al. (1997) find that a uniform $\text{Ro} = 0.5$ approximation (their Fig. 7 and Eq. 28) adequately captures the vorticity distribution in the descending branch of the winter Hadley cell in their simplified, dry GCM. And Zurita-Gotor and Held (2018) discuss the absolute vorticity distribution corresponding to uniform Ro .

²This does not emerge clearly in axisymmetric simulations, and on theoretical grounds in axisymmetric atmospheres φ_d should be poleward of $-\varphi_a$ (Hill et al. 2019).

Finally, though it does not enter into our model for the Hadley cell edges below, we present for a Boussinesq atmosphere (see e.g. Eq. 1 of Hill et al. (2019) for the full underlying system of equations) the depth-averaged potential temperature field in gradient balance with u_{Ro} (assuming u_{Ro} occurs near the tropopause while $u \approx 0$ at the surface). Denoted $\hat{\theta}_{\text{Ro}}$, it is given by

$$\frac{\hat{\theta}_a - \hat{\theta}_{\text{Ro}}(\varphi)}{\theta_0} = \frac{\text{Ro}}{2\text{Bu}} \left[(2 - \text{Ro}) \cos^2 \varphi + \cos^2 \varphi_a \times \right. \quad (6)$$

$$\left. \left(4(1 - \text{Ro}) \ln \left(\frac{\cos \varphi_a}{\cos \varphi} \right) + \text{Ro} \frac{\cos^2 \varphi_a}{\cos^2 \varphi} \right) \right]$$

where $\hat{\theta}_a$ is the depth-averaged potential temperature at the latitude φ_a , θ_0 is the Boussinesq reference potential temperature, and

$$\text{Bu} \equiv \frac{gH}{(\Omega a)^2} \quad (7)$$

is the planetary Burger number with gravity g and tropopause height H .

Fig. 1 shows example u_{Ro} , M_{Ro} , and $\hat{\theta}_{\text{Ro}}$ fields with $\text{Ro} = 1, 0.5$, or 0.3 and $\varphi_a = 0^\circ$ or 20° . For zonal wind, irrespective of Ro and φ_a , u_{Ro} must vanish at φ_a . If $\varphi_a = 0$, it increases monotonically moving toward either pole, with greater meridional shear the larger Ro is. If $\varphi_a \neq 0$, u_{Ro} is negative from $-\varphi_a$ to φ_a , minimizes at the equator, and increases monotonically toward either pole. Both moving φ_a off equator and decreasing Ro act to weaken the meridional shears. For example, at 30°S/N , $u_{\text{Ro}} \approx 133, 67$, and 40 m s^{-1} respectively for $\text{Ro} = 1, 0.5$, and 0.3 if $\varphi_a = 0$ or $71, 36$, and 21 m s^{-1} respectively if $\varphi_a = 20^\circ$. For angular momentum, irrespective of Ro and φ_a , M_{Ro} at φ_a is equal to the local planetary angular momentum $\Omega a^2 \cos^2 \varphi_a$. It decreases poleward thereof and, if $\varphi_a \neq 0$, increases equatorward to a maximum at the equator. For the gradient-balanced potential temperature, $\hat{\theta}_{\text{Ro}}$ maximizes at φ_a irrespective of Ro and φ_a and for $\varphi_a \neq 0$ has a local minimum at the equator. As Ro increases, the meridional temperature gradients increase in magnitude, with a deeper equatorial dip and a more equatorward shoulder poleward of φ_a where temperatures begin dropping rapidly toward the pole.

3. Combined theory for Hadley cell ascending and descending edges

Having defined the fixed- Ro fields, we now use them to derive our theory for φ_d , which closely follows that of KL12. We then introduce within it our scaling for φ_a , yielding our unified theory for φ_d and φ_a .

a. Baroclinic instability onset theory for the Hadley cell edge with $\text{Ro} < 1$

Following H00, the baroclinic instability criterion for the two-layer model is approximately

$$\frac{u}{\Omega a} = \text{Bu} \Delta_v \frac{\cos \varphi}{\sin^2 \varphi}, \quad (8)$$

where u is the zonal wind in the upper layer, the wind in the lower layer has been assumed small enough to neglect, and Δ_v is a static stability parameter representing the bulk fractional increase in potential temperature from the surface to the tropopause.^{3,4} H00 applies this to the annual-mean Hadley cells by assuming on-equatorial ascent, that the zonal winds are AMC, and that the descending edge is identical to this baroclinic instability onset latitude. Formally, taking $\varphi_a \approx 0$, using (2) for u in (8), and taking the small-angle limit yields the original H00 theory for φ_d , which we denote φ_{H00} :

$$\varphi_{\text{H00}} = (\text{Bu} \Delta_v)^{1/4}. \quad (9)$$

Using u_{Ro} (4) rather than u_{amc} (2) as the zonal-wind profile in (8), for $\text{Ro} < 1$ the predicted cell edge becomes

$$\varphi_{\text{Ro,ann}} = \left(\frac{\text{Bu}}{\text{Ro}} \Delta_v \right)^{1/4} = \text{Ro}^{-1/4} \varphi_{\text{H00}}, \quad (10)$$

with φ_{H00} given by (9). This displaces the cell edge prediction poleward by, for example, $\sim 19\%$ if $\text{Ro} = 0.5$ or $\sim 50\%$ if $\text{Ro} = 0.2$. Using the original $H = 10 \text{ km}$ and $\Delta_v = 1/8$ parameter values from Held and Hou (1980) yields $\text{Bu} \approx 0.46$ and $\varphi_{\text{H00}} \approx 28^\circ$, which becomes approximately 33.3° if $\text{Ro} = 0.5$ or 41.9° if $\text{Ro} = 0.2$. This poleward displacement as Ro decreases adheres to physical intuition: because the upper-layer zonal wind magnitude at each latitudes decreases as Ro decreases, the two-layer baroclinic instability onset criterion is met farther poleward.

For $\varphi_a \neq 0$, using (4) in (8) gives without approximation

$$\frac{\sin^4 \varphi_d}{\cos^2 \varphi_d} - \sin^2 \varphi_a \frac{\sin^2 \varphi_d}{\cos^2 \varphi_d} - \frac{\text{Bu} \Delta_v}{\text{Ro}} = 0, \quad (11)$$

where φ_d is the descending edge. From (10) the last term could equivalently be written $-\varphi_{\text{Ro,ann}}^4$. These arguments serve equally for the cross-equatorial, winter cell and the summer cell (provided it exists), depending on which cell the chosen Ro value is representative of. A corollary is

³H00 uses the symbol R to denote the planetary Burger number, which elsewhere (Held and Hou 1980; Hill et al. 2019) is used for the thermal Rossby number. To prevent confusion we use the more explicit notation Bu for the planetary Burger number and Ro_{th} for the thermal Rossby number.

⁴The tropopause depth H is assumed horizontally uniform and identical in the RCE state and in the presence of the large-scale circulation; see Hill et al. (2020) for justification.

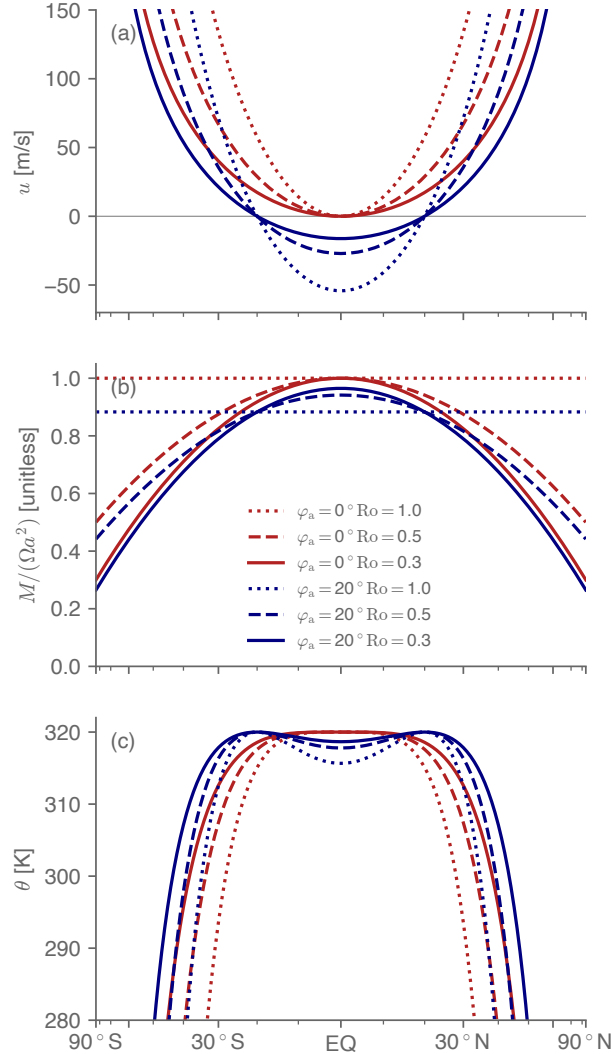


FIG. 1. Example (a) zonal wind (u_{Ro} , in m/s), angular momentum (M_{Ro} , normalized by Ωa^2 and thus unitless), and depth-averaged potential temperature (θ_{Ro} , units Kelvin) fields under a uniform Rossby number. Red curves are for $\varphi_a = 0^\circ$ and blue curves $\varphi_a = 20^\circ$ S/N, while dotted, dashed, and solid curves are for $Ro = 1.0, 0.5$, and 0.3 , respectively. Horizontal axis spacing is in $\sin \varphi$.

that if the mean Ro value is the same in both cells, then the Hadley circulation extends equally far into either hemisphere irrespective of φ_a . Note that our assumption of uniform Ro throughout either cell differs slightly from KL12, who assume $Ro = 1$ from the summer-hemisphere edge of the cross-equatorial cell to the equator, a uniform Ro value in the winter hemisphere, and a uniform Ro value throughout the summer cell.

We have performed a 2D parameter sweep over φ_a and $(Bu\Delta_v/Ro)^{1/4}$, from 0° to 90° in 1° increments for φ_a and from 0 to 2 in 0.01 increments for $(Bu\Delta_v/Ro)^{1/4}$, solving (11) numerically for each pair of parameter values. The results are shown as shaded contours in Fig. 2. The value of φ_d increases monotonically with φ_a and with $\varphi_{Ro,ann}$.

Close to the vertical axis of Fig. 2, $|\varphi_{Ro,ann}/\varphi_a| \gg 1$, and $\varphi_d \approx \varphi_{Ro,ann}$: φ_a is negligibly off-equator. Close to the horizontal axis of Fig. 2, $|\varphi_{Ro,ann}/\varphi_a| \ll 1$, and thus $\varphi_d \approx \varphi_a$. This regime usefully describes cases where the summer cell effectively disappears, as in all of the perpetual solstice simulations we will discuss below. For the winter hemisphere, the interpretation is that baroclinic instability onset occurs just poleward of $-\varphi_a$ near enough that it can be approximated as $-\varphi_a$. For intermediate values, if e.g. $\varphi_a \approx \varphi_{Ro,ann}$, then φ_d is displaced 27% poleward of φ_a . We note that $|\varphi_d| \geq |\varphi_a|$; the descending edge latitude is always at or poleward of the ascending edge latitude. This is as it should be for the summer-hemisphere φ_d but will

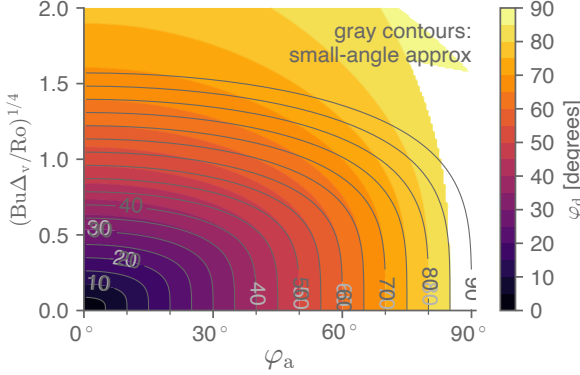


FIG. 2. Numerical solutions of (11) for values of φ_a and of $(\text{Bu}\Delta_v/\text{Ro})^{1/4}$, with φ_a sampled from 0 to 90 degrees latitude in 1-degree increments and $(\text{Bu}\Delta_v/\text{Ro})^{1/4}$ (which is dimensionless) from 0 to 2.0 in 0.01 increments. Areas in white indicate that the simple numerical algorithm used did not converge. Contours are from 5 to 90° in 5° increments according to the colorbar and also labeled in light gray. Overlaid dark gray contours and labels are the corresponding small-angle solutions obtained using (12).

prove imperfect for the winter φ_d in the idealized GCM simulations discussed below.

Making the small-angle approximation in (11) for φ_d and φ_a results in closed expression for φ_d :

$$\varphi_d^2 = \varphi_a^2 \left(\frac{1}{2} + \sqrt{\frac{1}{4} + \frac{\text{Bu}\Delta_v}{\text{Ro}\varphi_a^4}} \right) = \varphi_a^2 \left(\frac{1}{2} + \sqrt{\frac{1}{4} + \left(\frac{\varphi_{\text{Ro,ann}}}{\varphi_a} \right)^4} \right) \quad (12)$$

This small-angle approximation is shown as overlaid contours in Fig. 2. Only for $(\text{Bu}\Delta_v/\text{Ro})^{1/4} \gtrsim 0.8$ does the small-angle approximation error exceed a few degrees latitude, irrespective of φ_a .

b. Incorporating theory for φ_a

Using (12) requires knowledge of φ_a , which KL12 diagnose. Hill et al. (2021) derive a prognostic theory for φ_a based on the meridional extent of supercritical forcing, i.e. the latitude range within the summer hemisphere for which the gradient-balanced wind fields that would emerge absent a large-scale circulation given the forcing would be symmetrically unstable. Specifically,

$$\varphi_a = c_a \left(\frac{\text{Ro}_{\text{th}}}{2} \right)^{1/3}, \quad (13)$$

where c_a is an empirically determined fitting parameter and

$$\text{Ro}_{\text{th}} \equiv \text{Bu}\Delta_h \sin \varphi_m \quad (14)$$

is the thermal Rossby number, with Δ_h a parameter of the imposed forcing field that determines the bulk meridional

temperature gradients of the forcing in conjunction with φ_m , the latitude at which the forcing maximizes. For the solstitial, cross-equatorial Hadley cells in the simulations analyzed by Hill et al. (2021) the best-fit value of c_a ranges from 1.3 to 2.6 across three idealized GCMs.⁵ For Ro_{th} , Hill et al. (2021) show that for solstitial seasons one can attain an accurate estimate with φ_m set to 90° by tuning the value of Δ_h . Doing so, the non-standard $\sin \varphi_m$ term drops out and the Ro_{th} definition becomes the more conventional $\text{Ro}_{\text{th}} = \text{Bu}\Delta_h$. But the $\sin \varphi_m$ dependence is necessary for understanding the annual cycle as will be discussed further below.

Given diagnosed values of c_a and Ro for each Hadley cell, (13) in conjunction with (12) provide a theory for all three cell edges: (13) predicts φ_a , and using that in (12) for φ_d then yields

$$\varphi_d = c_d c_a \left(\frac{\text{Ro}_{\text{th}}}{2} \right)^{1/3} \sqrt{\frac{1}{2} + \sqrt{\frac{1}{4} + \frac{2^{4/3}}{c_a^4} \frac{\Delta_v}{\Delta_h \sin \varphi_m} \frac{1}{\text{Ro}\text{Ro}_{\text{th}}^{1/3}}}}, \quad (15)$$

where we have also included the empirical fitting parameter c_d that will prove necessary for the simulations analyzed below. The term $\Delta_v/\Delta_h \sin \varphi_m$ amounts to a seasonally varying bulk isentropic slope of the radiative-convective equilibrium state. From (15), the poleward edge of either Hadley cell increases with increasing Ro_{th} , increasing isentropic slope, or decreasing Ro . Large Ro_{th} corresponds to the large- φ_a limit above, $\varphi_d \approx \varphi_a$, while small Ro_{th} corresponds to the small- φ_a limit of $\varphi_d \approx \varphi_{\text{Ro,ann}}$.

4. Simulation results

We now assess the above theoretical arguments against simulations in two moist GCMs and one dry idealized GCM. After describing the models and simulations, we consider the annual cycles of φ_d and φ_a in an Earth-like aquaplanet control simulation, followed by their behaviors across a wide range of rotation rates in all three GCMs.

a. Description of models and simulations

Details of the model formulations and simulations are provided by Hill et al. (2021). Briefly, the dry model (Schneider 2004) approximates radiative transfer via Newtonian cooling, with the equilibrium temperature field that temperatures are relaxed toward being the forcing field from Lindzen and Hou (1988) but maximizing at the north pole. The relaxation field is statically unstable, and a simple convective adjustment scheme relaxes temperatures of unstable columns toward a specified lapse rate at a fixed

⁵Hill et al. (2021) report values for c_a of 1.0, 1.7, and 2.1 for the Faulk et al. (2017), Singh (2019), and (Hill et al. 2021) simulations, respectively, but these implicitly incorporate the $2^{-1/3} \approx 0.8$ factor in (13). We separate it out from c_a for better consistency with (13).

timescale of $\gamma\Gamma_d$, where $\Gamma_d = g/c_p$ is the dry adiabatic lapse rate with c_p the specific heat of dry air at constant pressure, and $\gamma = 0.7$ mimics the stabilizing effects of latent heat release that would occur in a moist atmosphere (though the model is otherwise dry). Four simulations are performed, three with the Δ_h parameter that determines the horizontal temperature gradients of the forcing set to 1/15 and with the planetary rotation rate set to 0.25, 1, or $2 \times$ Earth's value, and another with $\Delta_h = 1/6$ and Earth's rotation rate.

The moist simulations are those originally presented by Faulk et al. (2017) and Singh (2019). The Faulk et al. (2017) simulations use the idealized aquaplanet model of Frierson et al. (2006) with a slab-ocean lower boundary with a 10-m mixed layer depth. They are forced either with an annual cycle of insolation approximating that of present-day Earth, or with insolation fixed at northern solstice. The annual cycle simulations include planetary rotation rates ranging from 1/32 to $4 \times$ Earth's by factors of two, while the three perpetual solstice simulations are at 1, 1/8, or $1/32 \times$ Earth's rotation rate. The Singh (2019) simulations use an idealized aquaplanet close to that of O'Gorman and Schneider (2008), itself a modified version of the Frierson et al. (2006) model. All of these simulations use a time-invariant, solstitial insolation forcing as in the second subset of the Faulk et al. (2017) simulations, with rotation rates ranging from 1/8 to $8 \times$ Earth's.

The simulated values of φ_d are diagnosed conventionally as the latitude at which the mass-overturning streamfunction at the level of the cell center reaches 10% of its maximum value, with an additional $\cos \varphi$ weighting factor that accounts for constricting latitude circles moving poleward (Singh 2019). The 10% threshold is needed rather than a zero crossing for cases with large Hadley cells, in which the Ferrel cells and/or summer Hadley cell can be nonexistent and the streamfunction same-signed (albeit very weak) all the way to either pole. For φ_a , the same 10% threshold is used in the perpetual-solstice simulations and in the annual cycle simulations for months in which the summer Hadley cell has effectively vanished. In months where both Hadley cells are well defined, φ_a is taken as the average of the inner edges of the two cells computed using this 10% criterion (which is approximately the latitude of the streamfunction zero crossing; not shown).

b. Annual cycles of φ_a and φ_d

KL12 apply their theory to the seasonal (DJF, MAM, JJA, and SON) Hadley cell descending edges in CMIP3 GCMs, arguing that Ro and φ_a compensate with respect to φ_d : at solstice, φ_a is farthest poleward, which acts to move both the summer and winter φ_d poleward, but Ro is closest to unity in the solstitial cross-equatorial cell, which acts to move the winter φ_d equatorward. In our formalism,

by (15) if φ_a is small relative to $\varphi_{Ro,ann} = (Bu\Delta_v/Ro)^{1/4}$ throughout the annual cycle, then the annual cycle of φ_d is determined by the annual cycle of Ro (provided H that appears in Bu and Δ_v are constant across seasons). We now assess the seasonally forced simulation at Earth's rotation rate of Faulk et al. (2017), which turns out to follow effectively the opposite limit: φ_a variations (which are well predicted by supercriticality) with Ro = 1 assumed throughout the annual cycle account for the annual cycle of the winter φ_d .

Fig. 3 shows the climatological annual cycles of φ_a , φ_d in both hemispheres, and the meridional overturning streamfunction at 500 hPa, as well as theoretical estimates described below for each cell edge. The simulated cells are reasonably Earth-like in their meridional extent, overturning strength, and annual cycle phasing. In particular, φ_a (solid red curve) migrates into either summer hemisphere but with a roughly 1-month lag behind the insolation, and its seasonal migrations (25.7°S – 23.2°N) are several times larger than those of φ_d , (solid blue curves; 21.3 – 30.0°N and 21.7 – 26.5°S). Because the summer-hemisphere cell is so weak, φ_d is only well defined in the winter half-month for either hemisphere (December through May for the northern hemisphere, June through November for the southern hemisphere). Compared to Earth, the φ_a excursions into the summer hemisphere and cross-equatorial Hadley cell overturning strength are moderately excessive, while the simulated summer cell is too weak over most of the annual cycle. Finally, the transition from equinoctial to solstitial regimes is excessively rapid, approaching closer to the square-wave prediction of Lindzen and Hou (1988) for axisymmetric atmospheres than Earth's more sinusoidal variations (Dima and Wallace 2003); in fact the annual-mean (not shown) rainfall and Hadley cells both show a double ITCZ resulting from this rapid jumping of the ascent rather deep into either summer hemisphere. These discrepancies are likely due to the rather shallow 10-m mixed layer, leading to excessively rapid seasonal transitions (Donohoe et al. 2014; Wei and Bordoni 2018).

The insolation maximum (orange stars, lagged by 1 month for ease of comparison with φ_a), which corresponds to the forcing maximum latitude φ_m , occurs near the summer pole during the core solstitial months, whereas φ_a (solid red curve) stays within the tropics. In the other months of the year, $\varphi_a \approx \varphi_m$. The supercriticality scaling for φ_a (13) captures this. Specifically, we set $\Delta_h = 1/15$ uniformly throughout the annual cycle and take φ_m to be the insolation maximum latitude, lagged by 1 month to accommodate the system's thermal inertia.⁶ Setting $c_a \approx 1.8$

⁶Hill et al. (2020) diagnose Δ_h from latitude-by-latitude RCE simulations under annual-mean insolation and find $\Delta_h \approx 1/8$, roughly twice that of the $\Delta_h \approx 1/15$ value for RCE simulations under solstitial forcing from (Hill et al. 2021). Presumably then Δ_h would be even larger under equinoctial forcing. But we do not attempt to account for this seasonality in Δ_h .

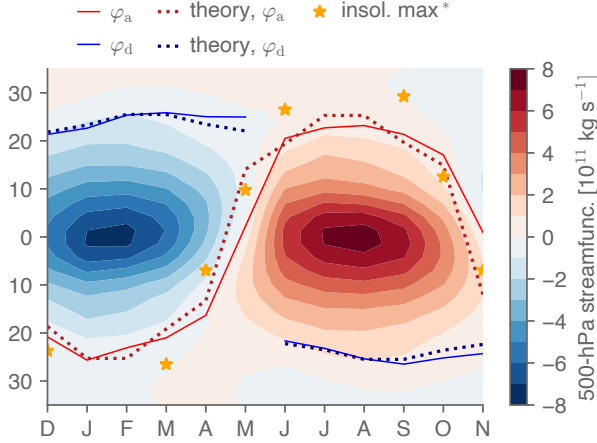


FIG. 3. In the seasonally forced, Earth-like aquaplanet simulation, climatological annual cycle of Hadley cell streamfunction at 500 hPa in shading according to the colorbar, as well as Hadley cell edges and theories for the Hadley cell edges as indicated in the legend. Note that the insolation maximum (orange stars) is shifted by one month to facilitate comparison with φ_a , and in the two months nearest solstice the maximum is near the summer pole and thus not shown.

for all months then yields a good approximation (dotted dark red curve) to the simulated φ_a . This value of c_a is $\sim 37\%$ larger than the best-fit value of 1.31 for the solstitial φ_a across the Faulk et al. (2017) seasonally forced simulations with different rotation rates—a neither trivial nor order-of-magnitude difference, suggesting that the proportionality is moderately influenced by different processes in these two distinct contexts. The 1.8 value is also less than the values of 2.2 and 2.6 diagnosed across rotation rates for, respectively, the simulations of Singh (2019) and the dry simulations of Hill et al. (2021).

We then use φ_a predicted as just described to predict φ_d as follows. Due to an inadvertent loss of zonal-wind data from the Faulk et al. (2017) simulations, we are not able to directly diagnose Ro . Instead, we assume $Ro = 1$, which provided $0 \leq Ro \leq 1$ yields the equatorward-most possible φ_d predictions, all else equal. Even still, this yields a φ_d prediction poleward of the simulated φ_d values (not shown), which we correct for by setting $c_d = 0.75$ in (15). We then shift the results later in time by 1-month, resulting in a considerably accurate fit to the simulations (dotted blue curve). In the concluding section below we provide speculative arguments to justify this equatorward displacement and 1-month phase lag of φ_d compared to φ_a . The φ_d is only marginally improved if the actual simulated φ_a values are used rather than our predicted φ_a (not shown).

These results suggest that relatively muted annual cycles of φ_d relative to that of φ_a can emerge via different mechanisms even restricting to a reasonably Earth-appropriate segment of the parameter space. In the comprehensive GCMs analyzed by KL12, φ_a presumably

varies closer to the real-world value and thus less than in our aquaplanet simulations, while the seasonal Ro values that KL12 indirectly diagnose as a fitting parameter range over 0.45–1. By (12), using $H = 10$ km, then for Earth $Bu \approx 0.46$, which with the standard $\Delta_v = 1/8$ value, φ_a ranging from the equator to 15° S/N, and these Ro ranges yields a maximal φ_d range of 28.0° ($\varphi_a = 0$, $Ro = 1$) to 35.9° ($\varphi_a = 15^\circ$, $Ro = 0.45$). But these values are fairly insensitive to both Ro and φ_a within these ranges: if Ro is kept at unity, the $\varphi_a = 15^\circ$ prediction moves equatorward only by 1.7° , and conversely if φ_a is at the equator the $Ro = 0.45$ prediction moves poleward by only 2.1° . Conversely, in our simulation the monthly variations of φ_d are comparable to the CMIP3 GCMs, $\lesssim 5^\circ$ about their annual means, but—with c_d and the 1-month lag from φ_a accounted for—appear determined almost entirely by the seasonality of φ_a with Ro constant.

c. Relative behaviors of solstitial φ_a and φ_d across rotation rates

In the small- Ro_{th} limit, (13) predicts $\varphi_a \propto Ro_{th}^{1/3}$, and Hill et al. (2021) show that this accurately describes the solstitial φ_a across planetary rotation rates in the idealized GCM simulations presently under consideration. For φ_d , by (11) for small Ro_{th} and thus small φ_a ,

$$\varphi_d \approx c_d \left(\frac{Bu \Delta_v}{Ro} \right)^{1/4} = c_d \left(\frac{Ro_{th} \Delta_v}{Ro \Delta_h} \right)^{1/4}, \quad (16)$$

again incorporating the empirical fitting parameter c_d . In that case, provided Ro does not change appreciably then $\varphi_d \propto Bu^{1/4} \sim Ro_{th}^{1/4}$, where in this context we can substitute Ro_{th} for Bu since only Ω is varied and appears identically (as Ω^{-2}) in the two nondimensional numbers. We now argue that the idealized GCM simulations reflect this modest $1/3 - 1/4 = 1/12$ difference in power-law exponent in Ro_{th} for φ_a vs. φ_d .

Fig. 4 shows the winter φ_d for all the simulations as a function of $Ro_{th}^{1/4}$. For each model, a best-fit line is included of φ_d with $Ro_{th}^{1/4}$ for simulations with $Ro_{th} < 2$. Overall the simulations follow this scaling well. Table 1 lists the slope and intercept from the linear best fits of φ_d against $Ro_{th}^{1/4}$, with the slope amounting to a best fit for the empirical c_d parameter in (15) (at least in the small- Ro_{th} limit). The inferred c_d values range from 1.4 for the Singh (2019) simulations to 0.9 for the Faulk et al. (2017) perpetual solstice simulations. The value of 1.0 for the Faulk et al. (2017) seasonal cycle simulations is modestly higher than the value discussed above of 0.8 for the climatological annual cycle in the Faulk et al. (2017) simulation at Earth's rotation rate—opposite to c_a , which was larger for the annual cycle than across rotation rates. The intercepts, which in theory should be zero, range from -2.4 to 5.6° latitude and average across the simulation sets to a modest 0.3° .

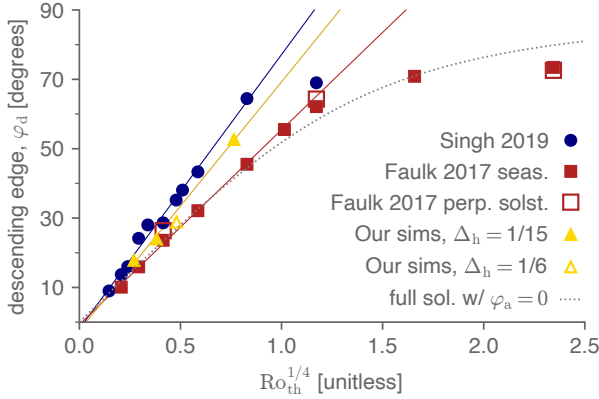


FIG. 4. Latitude of the winter-hemisphere descending edge of the cross-equatorial Hadley cell, φ_d , in idealized aquaplanet simulations of Faulk et al. (2017), Singh (2019), and in the idealized dry simulations of Hill et al. (2021) as a function of the thermal Rossby number to the one-fourth power, each signified by different symbols as indicated in the legend. The solid lines show the linear best fit for φ_d as a function of $Ro_{th}^{1/4}$ for the given simulation set, restricting to $Ro_{th} < 1$, with red, blue, and yellow for the Singh (2019), Faulk et al. (2017), and the $\Delta_h = 1/15$ dry simulations respectively. The dotted gray curve is the numerical solution to (11) with $\varphi_a = 0$ and $Ro\Delta_h/\Delta_v = 1$.

Table 1 includes best-fit power law exponents for φ_d and for φ_a against Ro_{th} computed for each set of simulations by linear regression in log-log space. For all sets of simulations, the inferred exponent is larger and closer to $1/3$ for φ_d than for φ_a , which is closer to $1/4$. The dry simulations exhibit the largest exponents for both, 0.41 and 0.3 , respectively, and the Faulk et al. (2017) seasonally forced and perpetual-solstice simulations, respectively, give the smallest exponents, 0.28 and 0.21 . The average of the best-fit exponents across the four simulation sets are nearly identical to the scalings, 0.26 and 0.33 .

As Ro_{th} increases beyond ~ 1 , the simulated φ_d level off, never exceeding $\sim 70^\circ$. The full, non-small-angle expression (11) solved numerically with $\varphi_a = 0$ and all parameters except Ω set to Earth-like values (dotted grey curve) qualitatively captures the leveling off of φ_d . This $\sim 70^\circ$ contrasts with φ_a , which in the slowly-rotating regime is near the summer pole (Hill et al. 2021). Table 1 includes the slope and intercepts of φ_a against $Ro_{th}^{1/3}$, with the slope amounting to a best fit for $c_a/2^{1/3}$ in (13). The ratio $2^{1/3}c_d/c_a$ takes values approximately over 0.6 - 1 in the four simulation sets. If Ro and the forcing isentropic slope Δ_v/Δ_h are both nearly unity, it can be shown from (13) and (16) that $\varphi_a = \varphi_d$ if $2^{1/3}c_d/c_a = Ro_{th}^{1/12}$. Given the 0.6 - 1 range for the left-hand-side, this yields $Ro_{th} \approx 1$, with φ_d equatorward of φ_a for larger Ro_{th} . This roughly captures the behavior of the simulations.

The unfilled yellow triangle in Fig. 4 shows the dry, LH88-forced simulation at Earth’s rotation rate and with $\Delta_h = 1/6$ rather than $\Delta_h = 1/15$ as in the other three dry

	winter φ_d			summer φ_a		
	power	c_d	intercept	power	$c_a/2^{1/3}$	intercept
theory	0.25	n/a	0°	0.33	n/a	0°
S19	0.25	1.4	-1.9°	0.32	1.8	-2.3°
F17, seas. forc.	0.26	1.0	5.6°	0.28	1.0	4.2°
F17, perp. solst.	0.21	0.9	-0.7°	0.30	1.1	4.4°
dry, LH88-forced	0.30	1.3	-2.4°	0.41	2.1	-9.2°
F17, ann. cyc.	n/a	0.8	n/a	n/a	1.8	n/a

TABLE 1. Best-fit exponents of power law scalings for the winter and summer edges of the cross-equatorial solstitial Hadley cell in each set of simulations, as well as the best-fit slope and intercepts for each simulation set against the theoretical Ro_{th} power law. The slope for φ_d amounts to an approximation of c_d and that of φ_a an approximation of c_a ; the latter is reported with the additional $2^{-1/3}$ factor included to facilitate direct comparison with c_d . Simulations are restricted to those for which $Ro_{th} < 2$, since the theoretical predictions of $1/3$ and $1/4$ for the winter and summer edges, respectively, assume small angle and thus small Ro_{th} . The dry LH88-forced simulations do not include the $\Delta_h = 1/6$ case. S19 stands for Singh (2019), and F17 stands for Faulk et al. (2017). The last row lists the diagnosed c_d and c_a values for the annual cycle in the Faulk et al. (2017) Earth-like simulation.

simulations. As is the case for φ_a (Hill et al. 2020), φ_d is somewhat separated from the power law of the $\Delta_h = 1/15$ cases. Strictly speaking, in the $\varphi_a \approx 0$ limit of (11), φ_d is independent of Δ_h . But, while small, $\varphi_a \neq 0$ in the simulations, and since an increase in Δ_h moves φ_a poleward, it is qualitatively consistent that φ_d moves poleward as a result. Given that the annual cycle amounts to a variation in $\Delta_h \sin \varphi_m$, it is worth noting that the slope between the $\Delta_h = 1/15$ and $\Delta_h = 1/6$ cases at Earth’s rotation rate is shallower than that inferred across rotation rates at $\Delta_h = 1/15$, which qualitatively coheres with c_d being smaller for the annual cycle than across rotation rates in the Faulk et al. (2017) simulations (Table 1).

Finally, to justify our assumption in the scaling for φ_d that the upper-tropospheric Ro within the Hadley cell can be treated as fixed, Fig. 5 shows the meridional profile of Ro at 300 hPa in each simulation of Singh (2019), computed both conventionally as (3) and, following Singh (2019), in a generalized form that incorporates vertical advection of angular momentum:

$$Ro_{gen} \equiv \frac{1}{f} \left[-\zeta + \frac{\omega}{v} \frac{\partial u}{\partial p} \right], \quad (17)$$

where v is meridional velocity, ω is vertical velocity in pressure coordinates, p is pressure, and all quantities are zonal averages. This accounts for the considerable tilting of streamlines, which causes the conventional Ro to deviate from unity even if streamlines and angular momentum contours are everywhere parallel. Though it is the conventional Ro that appears in u_{Ro} and thus ultimately our expressions for φ_d , for the simulations we argue that (17) is more instructive: for the two-layer model of baroclinic instability utilized, the bulk upper-tropospheric behavior is

more relevant than that at any chosen pressure level. And as streamlines begin tilting toward the surface in the descending branch, the conventional Ro at any given level decreases, while the bulk zonal velocities of the upper branch still roughly correspond to the planetary angular momentum values from where the streamlines exited the boundary layer in the ascending branch. In other words, along streamlines angular momentum is nearly conserved (see Fig. 7 of Singh (2019)), which the meridional profile of Ro at a fixed pressure level cannot capture.

The generalized Rossby number is close to unity over a large fraction of the cross-equatorial Hadley cell extent in all cases. (Both forms are masked out over 2°S – 2°N where division by the Coriolis parameter makes them less physically meaningful.) The difference made by the vertical advection term is particularly large in the ascending branches. For either version, we subjectively identify two regimes over the descending branch. Slowly rotating cases have Ro_{gen} relatively uniform or even increasing slightly from the equator to the winter descending edge. More rapidly rotating cases have Ro_{gen} decreasing poleward, approaching zero in the vicinity of the winter descending edge, but there is considerable scatter in the value of Ro_{gen} at the edge. Despite this variation in the Rossby number across the simulations, it is evidently small enough that taking the bulk Ro_{gen} value as fixed in our scalings does not introduce major error.

5. Conclusions

a. Summary

We have introduced a new theory for the latitude of the poleward, descending edge of either Hadley cell (ϕ_d) by combining the uniform-Rossby-number model of KL12—which uses a diagnosis of the ascending edge latitude (ϕ_a) to generalize the baroclinic instability-based model of H00 from annual-mean conditions to the annual cycle—with our recently presented theory for the ascending edge being set by the meridional extent of supercritical forcing (Hill et al. 2021). The theory predicts that ϕ_d is displaced poleward when Ro decreases or as ϕ_a moves poleward, and ϕ_a varies with the thermal Rossby number to the one-third power. But in the small-angle limit reasonable for Earth, the dependence on ϕ_a drops out and the scaling for ϕ_d predicts a one-fourth power dependence on the planetary Burger number, or equivalently on the thermal Rossby number provided the $\Delta_v/\Delta_h Ro$ remain fixed.

In an Earth-like, seasonally forced idealized aquaplanet simulation with a relatively shallow, 10-m mixed layer ocean depth, ϕ_a migrates rapidly to $\sim 25^\circ$ into either summer hemisphere, and this seasonal cycle is well captured by the supercriticality-based scaling. The summer cell is too weak for the summer ϕ_d to be meaningful, but the winter ϕ_d varies by only $\lesssim 5^\circ$ latitude about its mean position in either hemisphere. Our combined theory predicting ϕ_a

and ϕ_d captures this behavior with Ro kept at unity as in the original H00 model, but requires in place of Ro variations that the ϕ_d prediction be lagged by one month from that of ϕ_a .

In simulations across a wide range of planetary rotation rates in three idealized GCMs, both ϕ_d and ϕ_a adhere to the respective power-law exponents predicted by our theories in the relevant small thermal Rossby number regime. This, combined with a smaller proportionality constant for ϕ_d compared to ϕ_a , helps explain why at very slow rotation rates the solstitial Hadley cell ascends essentially at the summer pole but considerably equatorward of the winter pole, $\sim 70^\circ$, rather than being roughly symmetric in extent about the equator as for more rapidly rotating cases.

b. Discussion

How might a predictive theory for Ro be constructed? Hoskins et al. (2020) offer an intriguing perspective relating to the frequency of deep convection in the ascending branch. They argue that only when convection is sufficiently deep will there be upper-tropospheric meridional outflow that travels nearly inviscidly (i.e. with $Ro \approx 1$) toward either pole; at times and longitudes where deep convection is absent, they argue $Ro \approx 0$. Under those conditions, the time-mean, zonal-mean Ro field becomes a function of the spatial and temporal occurrence of deep convection in the ascending branch. This contrasts with the conventional, extratropically focused approach to Ro , wherein it is controlled by stresses from subtropical and mid-latitude eddies propagating into the deep tropics and breaking (Walker and Schneider 2006; Schneider 2006).

Vallis et al. (2015) speculate that Rossby waves are generated at the latitude of baroclinic instability onset, that these Rossby waves then propagate equatorward and break, and that the Hadley cell terminates at this wave-breaking latitude rather than the instability onset latitude. This equatorward displacement may relate to our need for the $c_d < 1$ parameter value to fit the ϕ_d annual cycle in the seasonally forced aquaplanet simulation. And the overall dynamics may help explain the 1-month lag for ϕ_d relative to ϕ_a required to capture the precise month-to-month behavior of ϕ_d : it takes a finite amount of time for the zonal winds in the descending branch to adjust to a change in ϕ_a in the opposite hemisphere, and so too for the Rossby wave development, propagation, and breaking.

At the same time, across rotation rates the best fit c_d parameters are greater than unity in some cases (Table 1), which is hard to square with this Rossby wave-based mechanism of Vallis et al. (2015). Moreover, the physical credibility of the two-layer model's critical shear criterion for baroclinic instability has been rightly questioned; a series of studies utilize a more comprehensive treatment of baroclinic instability to argue that ϕ_d occurs where the

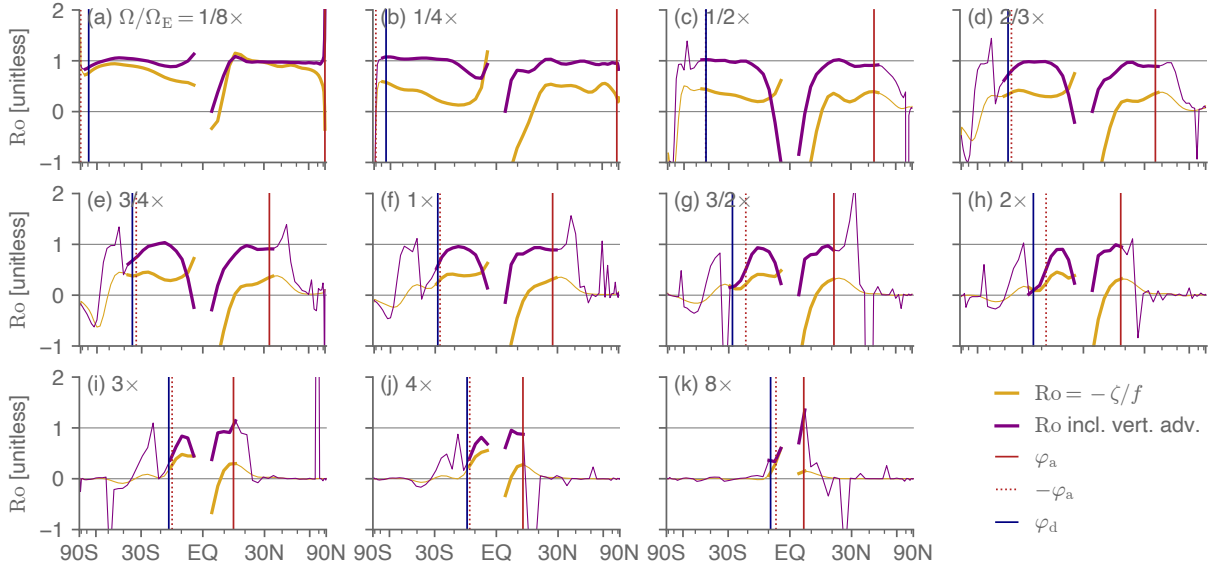


FIG. 5. Rossby number in the Singh (2019) simulations at the 300 hPa level, computed either conventionally using (3) or the generalized form (17) that accounts for the tilting of streamlines. Overlaid are the cell edges φ_a and φ_d , with $-\varphi_a$ also shown to ease comparison of the relative poleward extents of φ_a and φ_d . Rossby number values outside of the Hadley circulation are shown as thinner curves, since they are less relevant, and they are masked out within 2° of the equator where division by the Coriolis parameter makes them less meaningful.

vertical extent of baroclinic eddies spans a sufficient fraction of the troposphere (Korty and Schneider 2008; Levine and Schneider 2011, 2015). The same studies also incorporate the influence of moisture on the effective static stability, i.e. on Δ_v (Levine and Schneider 2011, 2015).

Though we have relied on Ro being uniform over the upper branch of each Hadley cell (c.f. KL12), the baroclinic instability criterion is computed latitude-by-latitude, and as such strictly speaking the behavior of Ro equatorward of the instability onset latitude is irrelevant. This also contrasts with the equal-area model appropriate for axisymmetric atmospheres, which depends on a measure of the potential temperature field integrated meridionally over the expanse of the cell.

Under annual-mean forcing in two dry and one moist idealized GCM, Mitchell and Hill (2021) find that φ_d scales as $\Omega^{-1/3}$ in all three models. This could be squared with our $\Omega^{-1/4}$ scaling for $\varphi_a = 0$ if Ro scales as $\Omega^{-2/3}$. By eye from their Fig. 8 and 10, Ro does indeed follow an exponent close to this in two of the models—the same dry GCM we use and the moist GCM used by Faulk et al. (2017). But a simpler dry dynamical core (Held and Suarez 1994) shows no clear dependence of Ro on Ω . Mitchell and Hill (2021) also put forward an “omega governor” mechanism which operates in the case that static stability and the effective heating (diabatic plus eddy heat convergence) averaged over the descending branch do not change. Under those conditions, the poleward extent and mass overturning rate of the Hadley cell must vary in tan-

dem: the cell weakens if it narrows, and it widens if it strengthens. Prior to any adjustment by φ_d , if φ_a moves poleward then the cell widens, which under the omega governor would act to strengthen the overturning. One can imagine that strengthening causing Ro to increase, insofar as parcels then traverse the upper branch more rapidly and hence are less exposed to eddy stresses. The increase in Ro would, all else equal, act to move φ_d equatorward, countering the direct influence of φ_a moving poleward.

Our theory could be further tested in numerous ways: against reanalysis data for the climatological annual cycle of the Hadley cells, against reanalysis data for inter-annual variability and trends, against comprehensive climate model simulations of global warming (c.f. KL12), and against simulations of other terrestrial planetary atmospheres.

Acknowledgments. We are grateful to Sean Faulk and Martin Singh for sharing the data from their simulations and for many valuable discussions. S.A.H. acknowledges financial support from NSF Award 1624740 and from the Monsoon Mission, Earth System Science Organization, Ministry of Earth Sciences, Government of India. J.L.M. acknowledges funding from the Climate and Large-scale Dynamics program of the NSF, Award 1912673.

References

Adam, O., T. Bischoff, and T. Schneider, 2016: Seasonal and Interannual Variations of the Energy Flux Equator and ITCZ. Part I: Zon-

- ally Averaged ITCZ Position. *J. Climate*, **29** (9), 3219–3230, doi:10.1175/JCLI-D-15-0512.1.
- Becker, E., G. Schmitz, and R. Geprags, 1997: The feedback of mid-latitude waves onto the Hadley cell in a simple general circulation model. *Tellus A*, **49** (2), 182–199, doi:10.1034/j.1600-0870.1997.t01-1-00003.x.
- Bordoni, S., and T. Schneider, 2008: Monsoons as eddy-mediated regime transitions of the tropical overturning circulation. *Nature Geosci*, **1** (8), 515–519, doi:10.1038/ngeo248.
- Byrne, M. P., and R. Thomas, 2019: Dynamics of ITCZ Width: Ekman Processes, Non-Ekman Processes, and Links to Sea Surface Temperature. *J. Atmos. Sci.*, **76** (9), 2869–2884, doi:10.1175/JAS-D-19-0013.1.
- Caballero, R., R. T. Pierrehumbert, and J. L. Mitchell, 2008: Axisymmetric, nearly inviscid circulations in non-condensing radiative-convective atmospheres. *Q.J.R. Meteorol. Soc.*, **134** (634), 1269–1285, doi:10.1002/qj.271.
- Dima, I. M., and J. M. Wallace, 2003: On the Seasonality of the Hadley Cell. *J. Atmos. Sci.*, **60** (12), 1522–1527, doi:10.1175/1520-0469(2003)060<1522:OTSOTH>2.0.CO;2.
- Donohoe, A., D. M. W. Frierson, and D. S. Battisti, 2014: The effect of ocean mixed layer depth on climate in slab ocean aquaplanet experiments. *Clim Dyn*, **43** (3–4), 1041–1055, doi:10.1007/s00382-013-1843-4.
- Faulk, S., J. Mitchell, and S. Bordoni, 2017: Effects of rotation rate and seasonal forcing on the ITCZ extent in planetary atmospheres. *J. Atmos. Sci.*, **74** (3), 665–678, doi:10.1175/JAS-D-16-0014.1.
- Frierson, D. M. W., I. M. Held, and P. Zurita-Gotor, 2006: A gray-radiation aquaplanet moist GCM. Part I: Static stability and eddy scale. *J. Atmos. Sci.*, **63** (10), 2548–2566, doi:10.1175/JAS3753.1.
- Guendelman, I., and Y. Kaspi, 2018: An Axisymmetric Limit for the Width of the Hadley Cell on Planets With Large Obliquity and Long Seasonality. *Geophysical Research Letters*, **45** (24), 13,213–13,221, doi:10.1029/2018GL080752.
- Held, I. M., 2000: The General Circulation of the Atmosphere. *The General Circulation of the Atmosphere: 2000 Program in Geophysical Fluid Dynamics*, No. WHOI-2001-03, Woods Hole Oceanog. Inst. Tech. Rept., Woods Hole Oceanographic Institution, 1–54.
- Held, I. M., and A. Y. Hou, 1980: Nonlinear axially symmetric circulations in a nearly inviscid atmosphere. *J. Atmos. Sci.*, **37** (3), 515–533, doi:10.1175/1520-0469(1980)037<0515:NASCIA>2.0.CO;2.
- Held, I. M., and M. J. Suarez, 1994: A Proposal for the Intercomparison of the Dynamical Cores of Atmospheric General Circulation Models. *Bull. Amer. Meteor. Soc.*, **75** (10), 1825–1830, doi:10.1175/1520-0477(1994)075<1825:APFTIO>2.0.CO;2.
- Hilgenbrink, C. C., and D. L. Hartmann, 2018: The Response of Hadley Circulation Extent to an Idealized Representation of Poleward Ocean Heat Transport in an Aquaplanet GCM. *J. Climate*, **31** (23), 9753–9770, doi:10.1175/JCLI-D-18-0324.1.
- Hill, S. A., S. Bordoni, and J. L. Mitchell, 2019: Axisymmetric constraints on cross-equatorial Hadley Cell extent. *J. Atmos. Sci.*, **76** (6), 1547–1564, doi:10.1175/JAS-D-18-0306.1.
- Hill, S. A., S. Bordoni, and J. L. Mitchell, 2020: Axisymmetric Hadley Cell theory with a fixed tropopause temperature rather than height. *J. Atmos. Sci.*, **77** (4), 1279–1294, doi:10.1175/JAS-D-19-0169.1.
- Hill, S. A., S. Bordoni, and J. L. Mitchell, 2021: Solsticial Hadley Cell Ascending Edge Theory from Supercriticality. *Journal of the Atmospheric Sciences*, **78** (6), 1999–2011, doi:10.1175/JAS-D-20-0341.1.
- Hoskins, B. J., G.-Y. Yang, and R. M. Fonseca, 2020: The detailed dynamics of the June–August Hadley Cell. *Quarterly Journal of the Royal Meteorological Society*, **n/a** (n/a), doi:10.1002/qj.3702.
- Kang, S. M., and J. Lu, 2012: Expansion of the Hadley Cell under global warming: Winter versus summer. *J. Climate*, **25** (24), 8387–8393, doi:10.1175/JCLI-D-12-00323.1.
- Korty, R. L., and T. Schneider, 2008: Extent of Hadley circulations in dry atmospheres. *Geophys. Res. Lett.*, **35** (23), L23 803, doi:10.1029/2008GL035847.
- Levine, X. J., and T. Schneider, 2011: Response of the Hadley Circulation to Climate Change in an Aquaplanet GCM Coupled to a Simple Representation of Ocean Heat Transport. *Journal of the Atmospheric Sciences*, **68** (4), 769–783, doi:10.1175/2010JAS3553.1.
- Levine, X. J., and T. Schneider, 2015: Baroclinic Eddies and the Extent of the Hadley Circulation: An Idealized GCM Study. *J. Atmos. Sci.*, **72** (7), 2744–2761, doi:10.1175/JAS-D-14-0152.1.
- Lindzen, R. S., and A. V. Hou, 1988: Hadley circulations for zonally averaged heating centered off the equator. *J. Atmos. Sci.*, **45** (17), 2416–2427, doi:10.1175/1520-0469(1988)045<2416:HCFZAH>2.0.CO;2.
- Mitchell, J. L., and S. A. Hill, 2021: Constraints from Invariant Subtropical Vertical Velocities on the Scalings of Hadley Cell Strength and Downdraft Width with Rotation Rate. *Journal of the Atmospheric Sciences*, **78** (5), 1445–1463, doi:10.1175/JAS-D-20-0191.1.
- O’Gorman, P. A., and T. Schneider, 2008: The hydrological cycle over a wide range of climates simulated with an idealized GCM. *J. Climate*, **21** (15), 3815–3832, doi:10.1175/2007JCLI2065.1.
- Rodwell, M. J., and B. J. Hoskins, 1996: Monsoons and the dynamics of deserts. *Q.J.R. Meteorol. Soc.*, **122** (534), 1385–1404, doi:10.1002/qj.49712253408.
- Schneider, T., 2004: The tropopause and the thermal stratification in the extratropics of a dry atmosphere. *J. Atmos. Sci.*, **61** (12), 1317–1340, doi:10.1175/1520-0469(2004)061<1317:TTATTS>2.0.CO;2.
- Schneider, T., 2006: The general circulation of the atmosphere. *Annu. Rev. Earth Planet. Sci.*, **34**, 655–688.
- Schneider, T., and S. Bordoni, 2008: Eddy-Mediated Regime Transitions in the Seasonal Cycle of a Hadley Circulation and Implications for Monsoon Dynamics. *J. Atmos. Sci.*, **65** (3), 915–934, doi:10.1175/2007JAS2415.1.
- Singh, M. S., 2019: Limits on the extent of the solsticial Hadley Cell: The role of planetary rotation. *J. Atmos. Sci.*, **76** (7), 1989–2004, doi:10.1175/JAS-D-18-0341.1.
- Vallis, G. K., P. Zurita-Gotor, C. Cairns, and J. Kidston, 2015: Response of the large-scale structure of the atmosphere to global warming. *Q.J.R. Meteorol. Soc.*, **141** (690), 1479–1501, doi:10.1002/qj.2456.
- Walker, C. C., and T. Schneider, 2006: Eddy influences on Hadley circulations: Simulations with an idealized GCM. *J. Atmos. Sci.*, **63** (12), 3333–3350, doi:10.1175/JAS3821.1.

- Watt-Meyer, O., and D. M. W. Frierson, 2019: ITCZ Width Controls on Hadley Cell Extent and Eddy-Driven Jet Position and Their Response to Warming. *J. Climate*, **32** (4), 1151–1166, doi:10.1175/JCLI-D-18-0434.1.
- Wei, H.-H., and S. Bordoni, 2018: Energetic Constraints on the ITCZ Position in Idealized Simulations With a Seasonal Cycle. *Journal of Advances in Modeling Earth Systems*, **10** (7), 1708–1725, doi:10.1029/2018MS001313.
- Zurita-Gotor, P., and I. M. Held, 2018: The Finite-Amplitude Evolution of Mixed Kelvin–Rossby Wave Instability and Equatorial Superrotation in a Shallow-Water Model and an Idealized GCM. *J. Atmos. Sci.*, **75** (7), 2299–2316, doi:10.1175/JAS-D-17-0386.1.